

Gravitational Wave Signatures of Quasi-Periodic Eruptions: LISA Detection Prospects for RX J1301.9+2747

Leif Lui,¹ Alejandro Torres-Orjuela,² Rudrani Kar Chowdhury,¹ and Lixin Dai^{1,*}

¹*Department of Physics, The University of Hong Kong, Pokfulam Road, Hong Kong*

²*Beijing Institute of Mathematical Sciences and Applications, Beijing 101408, China*

(Dated: August 12, 2025)

One prominent model for quasi-periodic eruptions (QPEs) is that they originate from extreme mass-ratio inspirals (EMRIs) involving stellar-mass objects orbiting around massive black holes and colliding with their accretion disks. We compute the gravitational wave signals from such a model, demonstrating that orbiter-disk interactions result in small frequency shifts and high-frequency tails due to the excitation of non-discrete modes. Interestingly, we show that QPE RX J1301.9+2747 could be detectable by future space-based gravitational wave detectors, provided a moderate eccentricity around 0.25 and a mass exceeding $35 M_{\odot}$ for the orbiter. Moreover, based on this QPE model, we show that the signal-to-noise ratio of the gravitational wave signals from QPEs, if detectable, will be sufficiently high to distinguish such systems from vacuum EMRIs and shed light on the origin of QPEs and environments around massive black holes.

Introduction—Quasi-periodic eruptions (QPEs) are a fascinating and relatively new phenomenon in high-energy astrophysics. As of now, about ten QPE sources have been identified across various galactic nuclei hosting massive black holes (MBHs) [1–10], and are characterized by luminous soft X-ray bursts ($\sim 10^{42-43} \text{ erg s}^{-1}$) lasting $\sim 1 \text{ ks}$, with quasi-periodic recurrence times of $\sim 10 - 100 \text{ ks}$ and variable flare luminosities.

QPEs have rapidly risen to prominence in high-energy astrophysics since their discovery, with their physical origin remaining unresolved and actively investigated. The proposed models include the transits of stellar-mass objects (SMOs) across an accretion disk, repeated partial tidal disruptions of an orbiting star, active-galactic-nuclei (AGN) disk instabilities, super-Eddington accretion disks with Lense-Thirring precession, mass transfer from an orbiting SMO to a MBH, gravitational lensing from close binary MBH systems, etc [11–21]. In this letter, we focus on the most well-studied “orbiter disk interaction” (ODI) model, in which the QPE flares are produced as a SMO closely orbits a MBH and continuously collides with the accretion disk of the MBH [22–26]. The ODI model is favored for its ability to naturally explain key observational features such as alternating flare amplitudes and quasi-periodic recurrence times. This quasi-periodicity arises as the SMO on a quasi-Keplerian orbit around a MBH iteratively traverses a longer arc followed by a shorter arc. This produces alternating time intervals between disk-crossing collisions that trigger flares, naturally creating the “long-short-long-short” recurrence pattern [24, 26].

While numerous models have been proposed to explain the electromagnetic (EM) signature of QPEs, their multi-messenger implications remain underexplored. Intriguingly, QPE systems described by the ODI model

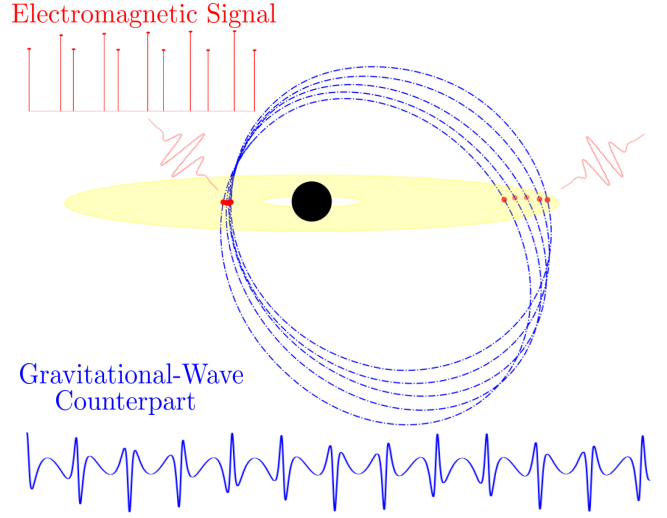


FIG. 1. Schematic depiction of an EMRI system where a SMO repeatedly collides with an accretion disk whilst orbiting a MBH. These collisions produce EM flares modulated by relativistic precession and orbital inclination. GWs emitted by the EMRI encode spacetime curvature perturbations, enabling multi-messenger probes of the orbital dynamics.

share key characteristics with extreme-mass-ratio inspirals (EMRIs), which are binaries where a SMO spirals towards a MBH emitting gravitational waves (GWs) [27]. We study these QPE/EMRI systems with ODIs, focusing on eccentric orbits ($e > 0$). Such systems are prime targets for space-based GW detectors like LISA, TianQin, and Taiji, operating in the frequency range $0.1-100 \text{ mHz}$ [28–32]. A joint EM-GW detection would establish QPEs as multi-messenger laboratories for probing accretion physics, strong-field gravity, and EMRI environments. FIG. 1 illustrates this framework, showing the interplay of EM signals from the ODI and the emis-

* Corresponding author: lixindai@hku.hk

sion of GWs from the EMRI. The ODIs extract energy and angular momentum from the EMRI, changing the morphology of the orbit and altering the EM and GW signals over observations.

Prior studies have provided estimates on the signal-to-noise ratio (SNR); however, no current work consistently includes ODI effects when computing the GW signals. Ref. [33–36] found that by treating current QPEs as vacuum EMRIs on nearly circular orbits, the SNRs are far too low to be detectable by space-based GW detectors. However, GW emission from eccentric binaries excites harmonics at higher frequencies, which can enhance detectability as they enter the sensitivity band of space-based detectors [37, 38]. While earlier work has suggested that high eccentricities might amplify GW signals from EMRIs, the applicability of this mechanism to QPEs remains unexplored [39]. Moreover, we find that ODIs excite non-discrete GW modes, which give rise to high-frequency tails. Although environmental effects have been demonstrated to enhance the detectability of GWs [8, 22, 23, 40, 41, 45], they have never been explored in the context of QPEs. In this paper, we account for these ODI effects and gauge the detectability of the GWs emitted by observed QPE candidates. Furthermore, we use the mismatch to determine whether the QPE GW signals can be differentiated from vacuum-EMRI GWs.

Observational Constraints of QPEs—The EM flares of the observed QPEs can be used to constrain the orbital information of the SMOs. In the ODI model, the SMO collides twice with the disk per orbit, and hence the recurrence timescale of QPE flares corresponds to roughly half of the orbital period of the SMO, which in turn allows one to calculate the frequency and strength of the GW signals. Another important parameter for the GW calculation is the eccentricity of the orbit, which can also be constrained using the pattern of the recurrence times observed in QPEs. Generally speaking, a tighter orbit, a higher eccentricity, and a larger SMO mass should enhance the detectability of GWs emitted by EMRIs.

Constraining QPE orbital parameters is complex due to degeneracies arising from relativistic precession. In this letter, we directly adopt the parameter-fitting results from Refs. [46, 47] in which the authors use accurate geodesic ray-tracing and Markov Chain Monte Carlo simulations. The orbital parameters are fitted using the data from XMM Newton, Chandra, eROSITA, Swift-XRT [6, 9, 10, 48–52], and align well with existing QPE literature [4, 7, 13, 46, 53, 54]. FIG. 2 shows the fitted orbital eccentricities e and frequencies f_{orb} by Refs. [46, 47], as well as the MBH masses M obtained from the $M - \sigma$ relation [55–57] for five observed QPEs.

Analyses treating QPEs as EMRIs (while not accounting for ODIs) suggest that QPEs with very low eccentricities ($e \lesssim 0.05$) [13, 51] do not produce GWs observable using space-based GW detectors. Indeed one sees in FIG. 2 that all QPE orbital frequencies are in the range

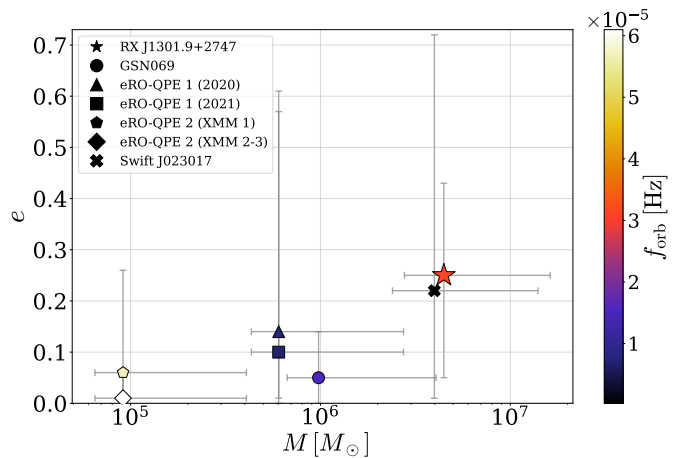


FIG. 2. EMRI parameters of five QPEs with data obtained from Ref. [47], where the x -axis is the MBH mass, and the y -axis is the orbital eccentricity. The color encodes the orbital frequency of the QPE, and the error bars are the $2\text{-}\sigma$ confidence interval.

0.01 – 0.1 mHz, placing the dominant mode of GW emission for circular orbits ($\omega_{\text{GW}} = 4\pi f_{\text{orb}}$) below the sensitivity band of space-based detectors [58, 59]. However, there exists a large uncertainty in the estimation of orbital parameters due to the limited number of cycles observed. The literature suggests that at least some QPEs can have moderate orbital eccentricities ($e \gtrsim 0.2$) [46, 47], which possibly generate GWs with a significant fraction of their higher harmonics lying inside the detection band [39, 60–63]. In this letter, we focus on the most promising case, RX J1301.9+2747, which has not only the largest reported orbital eccentricity ($e = 0.25^{+0.18}_{-0.20}$) but also a large number of observed cycles ($N \sim 10$). There is a large uncertainty in the SMO mass, as it does not alter the QPE’s periodicity due to the large mass ratio. Therefore, in our results, we use the entire mass range of SMO, as LIGO has detected the black holes in the intermediate mass range ($\mu \gtrsim 150 M_{\odot}$) [64].

We adopt the model by Ref. [46], which calculates the dynamical friction produced by a SMO crossing an accretion disk as

$$\delta \mathcal{E}_{\mu} = 4\pi \ln |\Lambda| \cdot \frac{G^2 \mu}{v^2} \cdot \frac{\Sigma}{\sin I}, \quad (1)$$

where $\delta \mathcal{E}_{\mu}$ is the energy dissipated per unit mass, μ is the SMO mass, v is the collision velocity, Σ is the surface density of the disk, I is the orbital inclination with respect to the equatorial plane, and $\Lambda = b_{\text{max}}/b_{\text{min}}$ is the ratio between the maximum and minimum impact parameter. We use $b_{\text{max}} = r_a$ and $b_{\text{min}} = r_s$, where r_a and r_s are radial distances from the apocenter of the orbit and the separatrix in Kerr spacetime, respectively [14].

Assuming that the quiescent luminosity between QPE flares stems from disk emission, we use the α -disk model

to model the disk's surface mass density [66]

$$\Sigma = 5.2\alpha^{-\frac{4}{5}} \dot{M}_{16}^{\frac{7}{10}} M^{\frac{1}{4}} R_{10}^{-\frac{3}{4}} f^{\frac{14}{5}}, \quad (2)$$

where $\dot{M}_{16} := \dot{M}/(10^{16} \text{ g s}^{-1})$ with \dot{M} denoting the accretion rate, M is the MBH mass, $R_{10} := R/(10^{10} \text{ cm})$ with R being the distance from the MBH, and α is the viscosity parameter for which we choose a fiducial value of 0.01. $f := (1 - \sqrt{GM/(2\eta R)})^{1/4}$ arises from the inner boundary condition ensuring that the viscous stress vanishes at the inner edge of the disk, and η is set to be 0.1, which is the standard accretion efficiency.

The large mass ratio between the MBH and the SMO allows us to calculate the SMO's trajectory and the associated GW emission using perturbative methods. The GWs of EMRIs can be computed using the Teukolsky equation [67–69], which consists of a wave operator \mathfrak{D} that describes the propagation of GWs through the curved spacetime of a rotating MBH, and a source term \mathfrak{T} that perturbs the spacetime [70–83]

$$\mathfrak{D}(\partial_\alpha, x^\alpha)[\psi] = \mathfrak{T}(x^\alpha), \quad (3)$$

where $x^\alpha = (t, \mathbf{x})$ are the spacetime coordinates, ∂_α are the partial derivatives with respect to x^α , and ψ is the rescaled Weyl scalar describing outgoing GWs. For EMRIs with MBH mass M and spin a as the primary, the Teukolsky wave operator in Boyer-Lindquist coordinates (t, r, θ, ϕ) is as follows

$$\begin{aligned} \mathfrak{D} = & \left[\frac{(r^2 + a^2)^2}{\Delta} - a^2 \sin^2 \theta \right] \partial_t^2 + \frac{4Mar}{\Delta} \partial_\phi \partial_t \\ & - \Delta^{-s} \partial_r (\Delta^{s+1} \partial_r) + \left[\frac{a^2}{\Delta} - \frac{1}{\sin^2 \theta} \right] \partial_\phi^2 \\ & - \frac{1}{\sin \theta} \partial_\theta [(\sin \theta) \partial_\theta] + 2s \left[\frac{a(r-M)}{\Delta} + i \csc \theta \cot \theta \right] \partial_\phi \\ & + 2s \left[\frac{M(r^2 - a^2)}{\Delta} - r - ia \cos \theta \right] \partial_t + (s^2 \cot^2 \theta + s), \end{aligned} \quad (4)$$

where $\Delta = r^2 - 2Ma + a^2$ and s is the spin weight ($s = -2$ for outgoing GWs). The rescaled Weyl scalar ψ can be constructed from the Weyl tensor $C_{\alpha\beta\gamma\delta}$ and the Kinnerley null tetrads $(l^\alpha, n^\alpha, m^\alpha, \bar{m}^\alpha)$ [84–86]

$$\psi = (r - ia \cos \theta)^4 C_{\alpha\beta\gamma\delta} n^\alpha \bar{m}^\beta n^\gamma \bar{m}^\delta. \quad (5)$$

Moreover, the source term is constructed by contracting the energy-momentum tensor $\mathcal{T}_{\alpha\beta}$ with l^α, m^α [67–69, 82]

$$\mathfrak{T} = 4\pi(r^2 + a^2 \cos^2 \theta) \mathcal{T}^{\alpha\beta} (l_\alpha l_\beta + l_\alpha m_\beta + m_\alpha m_\beta). \quad (6)$$

We model an EMRI with ODIs as a point-particle in Kerr spacetime that is perturbed by an ODI at (t_i, \mathbf{x}_i) . Therefore, $\mathcal{T}^{\alpha\beta} = \sum_i \mathcal{T}_i^{\alpha\beta}$ with

$$\mathcal{T}_i^{\alpha\beta} = \frac{\mu}{\sqrt{-g}} u_i^\alpha u_i^\beta \dot{\tau}_i \delta^3(\mathbf{x}(t) - \mathbf{x}_i) \Theta(t - t_i) \Theta(t_{i+1} - t), \quad (7)$$

where u^α is the 4-velocity of the point mass μ , $\delta^3(\cdot)$ is the 3-dimensional δ -Dirac distribution, $\Theta(\cdot)$ is the step-function, and the overdot denotes the derivative with respect to coordinate time t .

To incorporate ODIs into purely GW-driven inspirals, we use the **FastEMRIWaveforms** package [9–17, 19] to compute the adiabatic inspiral due to GW radiation [6, 7, 15] between disk collisions. Whenever the SMO crosses the disk, we update the Kerr geodesics constants of motion $(\mathcal{E}, \mathcal{L}_z, \mathcal{Q}) \rightarrow (\mathcal{E}', \mathcal{L}'_z, \mathcal{Q}')$ [98, 99] according to the ODI model

$$\mathcal{E}' = \mathcal{E} - \delta\mathcal{E}, \quad \mathcal{L}'_z = \mathcal{L}_z - \delta\mathcal{L}_z, \quad \mathcal{Q}' = \mathcal{Q} - \delta\mathcal{Q}. \quad (8)$$

Here $\delta\mathcal{E} = \delta\mathcal{E}_\mu$ is given by Eq. (1) while $\delta\mathcal{L}_z$ and $\delta\mathcal{Q}$ can be obtained by solving [6, 7, 15, 100]

$$\begin{pmatrix} \delta p \\ \delta e \\ \delta x_I \end{pmatrix} = \begin{pmatrix} \frac{\partial p}{\partial \mathcal{E}} & \frac{\partial p}{\partial \mathcal{L}_z} & \frac{\partial p}{\partial \mathcal{Q}} \\ \frac{\partial e}{\partial \mathcal{E}} & \frac{\partial e}{\partial \mathcal{L}_z} & \frac{\partial e}{\partial \mathcal{Q}} \\ \frac{\partial x_I}{\partial \mathcal{E}} & \frac{\partial x_I}{\partial \mathcal{L}_z} & \frac{\partial x_I}{\partial \mathcal{Q}} \end{pmatrix} \begin{pmatrix} \delta \mathcal{E} \\ \delta \mathcal{L}_z \\ \delta \mathcal{Q} \end{pmatrix}, \quad (9)$$

which is the mapping of the Kerr geodesic constants $(\delta\mathcal{E}, \delta\mathcal{L}_z, \delta\mathcal{Q})$ to the orbital parameters of quasi-Keplerian orbits $(\delta p, \delta e, \delta x_I)$ (p : the semi-latus rectum, e : the orbital eccentricity, $x_I := \cos I$: the cos of the inclination I) using the Jacobian matrix [101]. The system of equations in Eq. (9) is underdetermined, so two further constraints are imposed for this calculation. First, since the ODI is modeled as a drag, we assume this drag exerts forces parallel to the orbital motion, damping the SMO's velocity while not changing its direction i.e., I should remain constant or $\delta x_I = 0$. This approximation is valid in the thin-disk regime, when the SMO is immersed in the disk for a very short time, and the supersonic regime, where the disk's velocity is negligible compared to the SMO's orbital velocity [8]. Second, we use Kepler's equation $r = p/(1 + e \cos \chi)$ and set $\delta r = 0$, to prevent unphysical effects where the SMO abruptly changes its radial position after the ODI. This leads to $\delta p = p \cdot \delta e \cos \chi / (1 + \cos \chi)$. These calculations are done iteratively over LISA's planned 4-year operation time.

Imprints on GWs from Disk Collisions—GW radiation drives inspiral and circularization for EMRIs [37, 38]. The energy loss due to GW radiation causes the orbit to become more tightly bound, reducing the semi-major axis. The angular momentum loss damps eccentricity because GWs are emitted more strongly during close approaches in eccentric orbits. ODIs accelerate the inspiral, as shocks introduce additional orbital energy loss. While the energy dissipated in a single ODI is small compared to the orbital binding energy, over the course of tens of thousands of cycles, the total energy and angular momentum dissipated due to ODIs can accumulate and leave observable signatures on the GW signals. ODIs also accelerate circularization. For a Keplerian orbit, we have $p = \mathcal{L}_z^2/M$ and $e^2 = 1 + 2\mathcal{E}\mathcal{L}_z^2/M^2$. The orbital eccentricity varies as $\delta e = (p/M \cdot \delta\mathcal{E} - (1 - e^2)/\sqrt{pM} \cdot \delta\mathcal{L}_z)/e$.

The first term dominates because p amplifies ODI energy perturbations while suppressing angular momentum effects, as $\delta\mathcal{E}$ and $\delta\mathcal{L}_z$ are of similar order of magnitude. Therefore, ODIs reduce e by introducing a negative $\delta\mathcal{E}$ effect which accelerates the orbital circularization.

We plot in FIG. 3 the characteristic strain for RX J1301.9+2747 using the minimal and maximal eccentricities constrained using QPE signals ($e_0 = 0.05, 0.43$, see FIG. 2), considering a vacuum EMRI and an EMRI with ODIs. One can see that the more eccentric orbit with $e_0 = 0.43$ can place the higher harmonics into LISA’s detectability band, and the ODIs amplify the power of the spectrum at these discrete higher harmonics. Moreover, the spectra for EMRIs with ODIs have high-frequency tails of non-discrete modes. This improves the GW detectability by enhancing the power of the spectrum at higher frequencies, as the characteristic strain for EMRIs with ODIs is higher than that of vacuum EMRIs.

To understand the GW waveform of EMRIs with ODIs, we consider a simple case where an EMRI abruptly changes its orbital frequency, semi-latus rectum, and eccentricity. This alters the GW frequencies ω_{nmk} and amplitude $\mathcal{A}_{\ell nmk}$, where ℓ is the orbital angular momentum mode index, and n, m , and k , are the radial, azimuthal, and polar mode indices, respectively. For vacuum EMRIs, the strain can be written as a sum of multiple modes with amplitudes $\mathcal{A}_{\ell nmk}$ and phases Φ_{nmk}

$$h(t) \propto \sum_{\ell, m, n, k} \mathcal{A}_{\ell nmk}(t) e^{-i\Phi_{nmk}(t)}. \quad (10)$$

If there is a sudden change in the frequency $\omega_{nmk} := d\Phi_{nmk}/dt$ from ω_{nmk} to $\omega'_{nmk} = \omega_{nmk} + \delta\omega_{nmk}$ and a sudden change in amplitude $\mathcal{A}'_{\ell nmk} = \mathcal{A}_{\ell nmk} + \delta\mathcal{A}_{\ell nmk}$ at $t = t_c$, the integral for the Fourier transform needs to be split into two parts, one $-\infty < t < t_c$ and another $t_c < t < \infty$. Using the stationary phase approximation and the Sokhotski-Plemelj theorem, the result is a frequency spectrum $\tilde{h}(\omega) \propto \sum_{\ell, m, n, k} \tilde{h}_{\ell nmk}$ split into three parts

$$\begin{aligned} \tilde{h}_{\ell nmk} = & \tilde{\mathcal{A}}_{\ell nmk}(\omega) \delta(\omega - \omega_{nmk}) + \tilde{\mathcal{A}}'_{\ell nmk}(\omega) \delta(\omega - \omega'_{nmk}) \\ & + \frac{e^{-i\omega_{nmk} t}}{i\omega} \left(\delta\tilde{\mathcal{A}}_{\ell nmk}(\omega) + \frac{\delta\omega}{\omega} \tilde{\mathcal{A}}_{\ell nmk}(\omega) \right). \end{aligned} \quad (11)$$

The first and second terms in Eq. (11) correspond to the GW fundamental frequencies and their mode shifts due to the altered dynamics, respectively, where the tildes denote the Fourier transform. From FIG. 3, one sees that the lower harmonics of EMRIs with ODIs align with those of vacuum EMRIs without a clear splitting of the GW modes. This is because the shifts in the fundamental frequencies ω_{nmk} are small, as $\delta\omega_{nmk} \propto p^{-5/2} \delta p$ and the shift in semi-latus rectum is small $\delta p/p \sim 10^{-5}$ for EMRIs far from the merger. The non-discrete (‘noisy’) part of the spectrum for EMRIs with ODIs corresponds to the last term in Eq. (11). It stems from discrete reductions in $(\mathcal{E}, \mathcal{L}_z, \mathcal{Q})$ during ODIs (cf. Eq. (8)), which

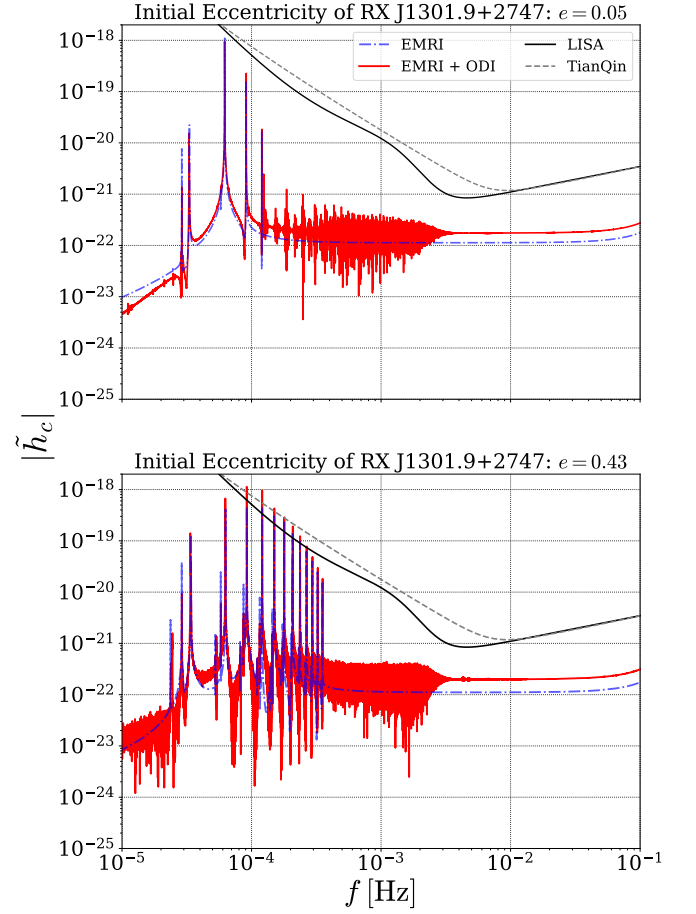


FIG. 3. The characteristic strain over LISA’s operation time of four years for a vacuum EMRI (dashed blue line) versus an EMRI with ODIs (solid red line) using the smallest (top panel) and largest (bottom panel) inferred initial eccentricity $e_0 = 0.25^{+0.18}_{-0.20}$ of RX J1301.9+2747 with the noise curves of LISA (black line) and TianQin (dashed gray line). The initial parameters are $M = 4.47 \times 10^6 M_\odot$, $\mu = 30 M_\odot$, $a = 0.9$, $p_0 = 55.5M(1 - e_0^2)$, $x_0 = \cos I_0 = 0.63$, and the luminosity distance $d_L = 100$ Mpc.

cause abrupt declines in p and e , and give rise to high-frequency tails commonly seen in EMRI glitches and the ringdown phase [20–24]. This effect is analogous to striking a bell, where the impulse excites vibrations at multiple frequencies, producing a transient “ring” that decays over time. This interpretation is consistent with our model, as the impulsive deceleration of the SMO during an ODI excites transient oscillations in the GW signal, differing from the scenario of vacuum EMRIs in which p and e evolve smoothly under gravitational radiation.

Detectability of GWs from QPEs—We use LISA’s power spectral density (PSD) [31, 60, 62, 63] and the luminosity distance $d_L = 100$ Mpc from observations [105] to compute the SNR of an EMRI with ODIs and its match with a vacuum EMRI with otherwise equal parameters. The detectability of a GW signal h is quantified

by its optimal SNR [63, 106]

$$\rho = \sqrt{\langle \tilde{h} | \tilde{h} \rangle}, \quad (12)$$

where $\langle \tilde{h} | \tilde{h} \rangle := 4\Re \left\{ \int_{f_{\text{low}}}^{f_{\text{high}}} df \tilde{h}^*(f) \tilde{h}(f) / S_n(f) \right\}$ is the noise-weighted inner product of the Fourier transformed waveforms \tilde{h} and \tilde{h} , $f_{\text{low}} \leq f \leq f_{\text{high}}$ is the frequency range of the detector (we use $f_{\text{low}} = 0.1$ mHz and $f_{\text{high}} = 100$ mHz), and S_n is the PSD of the noise. An EMRI is usually considered to be detectable by space-based detectors if $\rho \geq 20$ [107].

The similarity between the waveforms of the ODI-perturbed EMRIs h and vacuum EMRIs \bar{h} is quantified by their match \mathcal{M} [108–111]

$$\mathcal{M}(h, \bar{h}) = \frac{1}{\sqrt{\rho\bar{\rho}}} \langle \tilde{h} | \tilde{\bar{h}} \rangle, \quad (13)$$

and we can determine whether the two GW signals are distinguishable by the “rule-of-thumb” criteria [112]

$$\rho > \sqrt{\frac{D}{2(1-\mathcal{M})}}, \quad (14)$$

where $D \approx 15$ is the number of source parameters. In FIG. 4, we show the SNR of RX J1301.9+2747 for varying MBH mass M , SMO mass μ , and initial eccentricity e_0 . We adopt the M and e_0 inferred in Ref. [47], and consider μ in the entire range of SMOs ($1\text{--}100 M_\odot$), as μ is not well constrained from QPE observations. We use the current inferred orbital parameters from Refs. [46, 47], instead of the projected values for mid-2030s detectors, as these parameters deviate slowly over 10 years (see Supplementary Materials [101]). Also, our extended parameter space in FIG. 4 already accounts for these projected orbital parameters. The SNR increases with M , μ , and e_0 , as $|h_c| \propto \mu M$, and larger values for e_0 give rise to higher harmonics which are pushed into the sensitivity band of LISA. From the bottom panel of FIG. 4, we see that RX J1301.9+2747 will be detectable through GWs if $\mu \gtrsim 35 M_\odot$ for almost all M considered if $e_0 = 0.25$, while ρ can go over 800 for $M \gtrsim 10^7 M_\odot$ and $\mu \gtrsim 80 M_\odot$. However, even with lower SMO masses of $\mu \approx 10\text{--}20 M_\odot$, the QPE GW could still be detected if $e_0 \gtrsim 0.3$ and $M = 4.47 \times 10^6 M_\odot$ (cf. top panel of FIG. 4). Finally, we see from the middle panel of FIG. 4, that for $\mu = 30 M_\odot$ EMRIs with $M \gtrsim 3 \times 10^6 M_\odot$ will be detected if $e_0 \approx 0.5$. For almost all cases where a QPE emits detectable GWs, the SNR is also high enough to be differentiated from vacuum EMRIs. Conducting the same SNR and mismatch calculation using TianQin’s noise curve yields sub-detection SNRs. This is not surprising as TianQin is less sensitive to sources that emit low-frequency GWs (see FIG. 3), those being more massive MBHs. However, TianQin may still prove to be useful for detecting QPEs sources that host low-mass MBHs [29, 59].

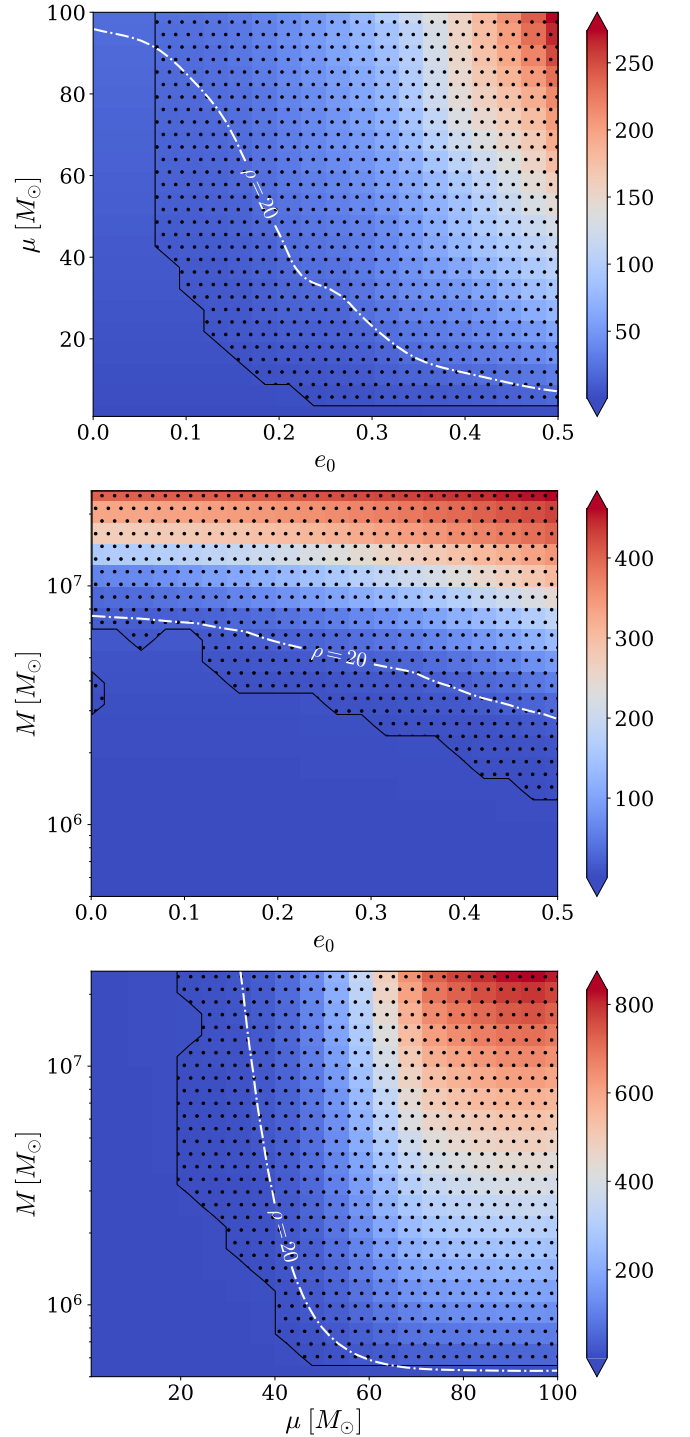


FIG. 4. The SNR of an EMRI with ODIs for varying μ and e_0 (top panel), M and e_0 (middle panel), and M and μ (bottom panel), assuming fiducial values $\mu = 30 M_\odot$, $M = 4.47 \times 10^6 M_\odot$, and $e_0 = 0.25$, respectively. The luminosity distance and the cosine of the initial orbital inclination angle are kept at $d_L = 100$ Mpc and $x_0 = 0.63$ for all sources considered, respectively. The white dashed-dotted line marks where the threshold SNR $\rho = 20$ is surpassed, and the hatched region indicates the parameter space where ρ is high enough to differentiate between an EMRI with ODIs and one in vacuum (cf. Eq. 14).

Discussion and Conclusion—In this letter, we present new calculations of GW signals from QPEs, a recently discovered astronomical phenomenon originating from MBHs, with its physical origin still under debate. By modeling the QPE bursts as EMRIs perturbed by repeated disk encounters, we novelly incorporate ODI physics into our GW computations. Our results show that ODIs in QPE significantly alter the GW signatures, enabling potential differentiation from vacuum EMRIs.

Our findings suggest that QPE RX J1301.9+2747 is a promising candidate for generating GW signals detectable by LISA within a region of its observationally constrained orbital parameter space. This demonstrates the potential of QPEs as multi-messenger sources, especially with the upcoming launches of space-based GW observatories, such as LISA, TianQin, and Taiji. Future simultaneous detection of EM and GW signals from QPEs will play a crucial role in elucidating their physical origins and advancing our understanding of gaseous and stellar environments around MBHs.

Future Work—Future works could apply this GW model to infer QPE parameters via match-filtering and Bayesian parameter estimation, which requires full GW templates. This is currently infeasible due to the high computational cost of waveform generation (from the inspiral pre-computation). Near-identity transformations (NITs) could accelerate the inspiral computation [113–117] through averaging and interpolation. However, as an averaging method, NITs are better suited for continuous dissipative forces (i.e., drag in gaseous halos) than discrete interactions like the ODIs considered in our work.

Moreover, our data analysis does not fully address the degeneracy problem, where vacuum-EMRI GW signals with different orbital parameters can mimic an ODI-perturbed GW signal. Therefore, the mismatch criterion in Eq. (4) represents an optimistic value. We intend to explore ways to decouple the degeneracies in GW signals by combining GW parameter estimation with the constraints from the QPE counterparts in future work.

Acknowledgment—We thank Xian Chen, Conor Dyson, Pau Amaro-Seone, Zhen Pan, Yi-Ming Hu, Tom Kwan, Samson Leong, Lars Lund Thomsen, and Zijian Zhang for the discussions. We acknowledge support from the National Natural Science Foundation of China and the Hong Kong Research Grants Council (N_HKU782/23, 17305523). LL is a Jockey Club Scholar supported by the Hong Kong Jockey Club and the Institute of Philanthropy (Hong Kong). ATO acknowledges support from the Key Laboratory of TianQin Project (Sun Yat-sen University), Ministry of Education (China).

[1] Karas, V. and Šubr, L., *A&A* **376**, 686 (2001).

[2] V. Karas and L. Subr, eConf **C041213**, 2103 (2004).

[3] L. Subr, V. Karas, and J. M. Hure, *Mon. Not. Roy. Astron. Soc.* **354**, 1177 (2004).

[4] T. Wevers *et al.*, *Monthly Notices of the Royal Astronomical Society* **471**, 1694 (2017).

[5] R. Arcodia *et al.*, *Nature* **592**, 704 (2021).

[6] G. Miniutti *et al.*, *Nature* **573**, 381 (2019).

[7] T. Wevers *et al.*, *Monthly Notices of the Royal Astronomical Society* **487**, 4136 (2019).

[8] J. Chakraborty, E. Kara, M. Masterson, M. Giustini, G. Miniutti, and R. Saxton, *Astrophys. J. Lett.* **921**, L40 (2021).

[9] G. Miniutti, M. Giustini, R. Arcodia, R. D. Saxton, A. M. Read, S. Bianchi, and K. D. Alexander, *Astron. Astrophys.* **670**, A93 (2023).

[10] G. Miniutti, M. Giustini, R. Arcodia, R. D. Saxton, J. Chakraborty, A. M. Read, and E. Kara, *Astron. Astrophys.* **674**, L1 (2023).

[11] A. King, *Monthly Notices of the Royal Astronomical Society* **493**, L120 (2020).

[12] P. Suková, M. Zajaček, V. Witzany, and V. Karas, *The Astrophysical Journal* **917**, 43 (2021).

[13] J. Xian, F. Zhang, L. Dou, J. He, and X. Shu, *The Astrophysical Journal Letters* **921**, L32 (2021).

[14] A. Ingram, S. E. Motta, S. Aigrain, and A. Karastergiou, *Monthly Notices of the Royal Astronomical Society* **503**, 1703 (2021).

[15] A. King, *Monthly Notices of the Royal Astronomical Society* **515**, 4344 (2022).

[16] J. H. Krolik and I. Linial, *Astrophys. J.* **941**, 24 (2022).

[17] B. D. Metzger, N. C. Stone, and S. Gilbaum, *The Astrophysical Journal* **926**, 101 (2022).

[18] M. Wang, J. Yin, Y. Ma, and Q. Wu, *The Astrophysical Journal* **933**, 225 (2022).

[19] J.-H. Chen, R.-F. Shen, and S.-F. Liu, *The Astrophysical Journal* **947**, 32 (2023).

[20] W. Lu and E. Quataert, *Monthly Notices of the Royal Astronomical Society* **524**, 6247 (2023).

[21] M. Middleton *et al.*, *Monthly Notices of the Royal Astronomical Society* **537**, 1688 (2025).

[22] W. H. Zurek, A. Siemiginowska, and S. A. Colgate, *Astrophys. J.* **434**, 46 (1994).

[23] L. Dai and R. D. Blandford, *Mon. Not. Roy. Astron. Soc.* **434**, 2948 (2013).

[24] A. Franchini, M. Bonetti, A. Lupi, G. Miniutti, E. Bortolas, M. Giustini, M. Dotti, A. Sesana, R. Arcodia, and T. Ryu, *Astron. Astrophys.* **675**, A100 (2023).

[25] I. Linial and B. D. Metzger, *Astrophys. J.* **957**, 34 (2023).

[26] I. Linial and B. D. Metzger, *The Astrophysical Journal Letters* **963**, L1 (2024).

[27] P. Amaro-Seoane, *Living Reviews in Relativity* **21**, 10.1007/s41114-018-0013-8 (2018).

[28] M. Colpi *et al.*, *arXiv e-prints*, arXiv:2402.07571 (2024).

[29] J. Mei *et al.*, *Progress of Theoretical and Experimental Physics* **2021**, 05A107 (2021).

[30] X. Gong *et al.*, in *Journal of Physics Conference Series*, Journal of Physics Conference Series, Vol. 610 (2015) p. 012011, arXiv:1410.7296 [gr-qc].

[31] A. Torres-Orjuela, S.-J. Huang, Z.-C. Liang, S. Liu, H.-T. Wang, C.-Q. Ye, Y.-M. Hu, and J. Mei, *Science China Physics, Mechanics, and Astronomy* **67**, 259511 (2024).

[32] A. Torres-Orjuela, in *7th International Workshop on the TianQin Science Mission* (2024) arXiv:2407.11293 [astro-ph.HE].

[33] X. Chen, Y. Qiu, S. Li, and F. K. Liu, *Astrophys. J.* **930**,

- 122 (2022).
- [34] S. Kejriwal, V. Witzany, M. Zajaček, D. R. Pasham, and A. J. K. Chua, *Monthly Notices of the Royal Astronomical Society* **532**, 2143 (2024).
- [35] T. F. M. Spieksma and E. Cannizzaro, *In the grip of the disk: dragging the companion through an agn* (2025), [arXiv:2504.08033 \[astro-ph.GA\]](#).
- [36] Y. Zhan, D. Wang, S.-X. Yi, and F.-Y. Wang, *Precise hubble constant measurement from quasi-periodic eruptions as electromagnetic counterparts to extreme mass ratio inspirals* (2025), [arXiv:2506.14150 \[astro-ph.HE\]](#).
- [37] P. C. Peters and J. Mathews, *Phys. Rev.* **131**, 435 (1963).
- [38] P. C. Peters, *Phys. Rev.* **136**, B1224 (1964).
- [39] P. Amaro-Seoane, J. R. Gair, M. Freitag, M. Coleman Miller, I. Mandel, C. J. Cutler, and S. Babak, *Class. Quant. Grav.* **24**, R113 (2007).
- [40] A. Torres-Orjuela, X. Chen, and P. Amaro Seoane, *Phys. Rev. D* **104**, 123025 (2021).
- [41] A. Torres-Orjuela, P. Amaro Seoane, Z. Xuan, A. J. K. Chua, M. J. B. Rosell, and X. Chen, *Phys. Rev. Lett.* **127**, 041102 (2021).
- [22] K. Destounis, A. G. Suvorov, and K. D. Kokkotas, *Phys. Rev. Lett.* **126**, 141102 (2021).
- [23] M. De Amicis, S. Albanesi, and G. Carullo, *Phys. Rev. D* **110**, 104005 (2024).
- [8] F. Duque, S. Kejriwal, L. Sberna, L. Speri, and J. Gair, *Phys. Rev. D* **111**, 084006 (2025).
- [45] C. Dyson, T. F. M. Spieksma, R. Brito, M. van de Meent, and S. Dolan, *Phys. Rev. Lett.* **134**, 211403 (2025).
- [46] C. Zhou, L. Huang, K. Guo, Y.-P. Li, and Z. Pan, *Phys. Rev. D* **109**, 103031 (2024).
- [47] C. Zhou, B. Zhong, Y. Zeng, L. Huang, and Z. Pan, *Probing orbits of stellar mass objects deep in galactic nuclei with quasi-periodic eruptions – ii: population analysis* (2024), [arXiv:2405.06429](#).
- [48] G. C. Dewangan, K. P. Singh, Y. D. Mayya, and G. C. Anupama, *Monthly Notices of the Royal Astronomical Society* **318**, 309 (2000).
- [49] P. A. Evans *et al.*, *Nature Astronomy* **7**, 1368–1375 (2023).
- [50] M. Guolo *et al.*, *Nature Astronomy* **8**, 347–358 (2024).
- [51] D. R. Pasham *et al.*, *The Astrophysical Journal Letters* **963**, L47 (2024).
- [52] J. Chakraborty *et al.*, *The Astrophysical Journal* **965**, 12 (2024).
- [53] N. C. Stone and B. D. Metzger, *Monthly Notices of the Royal Astronomical Society* **455**, 859 (2015).
- [54] C. S. Kochanek, *Monthly Notices of the Royal Astronomical Society* **458**, 127 (2016).
- [55] S. M. Faber and R. E. Jackson, *Astrophys. J.* **204**, 668 (1976).
- [56] N. J. McConnell, C.-P. Ma, K. Gebhardt, S. A. Wright, J. D. Murphy, T. R. Lauer, J. R. Graham, and D. O. Richstone, *Nature* **480**, 215 (2011).
- [57] J. Kormendy and L. C. Ho, *Annual Review of Astronomy and Astrophysics* **51**, 511–653 (2013).
- [58] P. Amaro-Seoane *et al.*, *Living Reviews in Relativity* **26**, 2 (2023).
- [59] E.-K. Li *et al.*, *arXiv e-prints*, [arXiv:2409.19665](#) (2024).
- [60] N. J. Cornish and L. J. Rubbo, *Phys. Rev. D* **67**, 022001 (2003).
- [61] L. Barack and C. Cutler, *Phys. Rev. D* **75**, 042003 (2007).
- [62] A. Klein, E. Barausse, A. Sesana, A. Petiteau, E. Berti, S. Babak, J. Gair, S. Aoudia, I. Hinder, F. Ohme, and B. Wardell, *Phys. Rev. D* **93**, 024003 (2016).
- [63] W.-F. Feng, H.-T. Wang, X.-C. Hu, Y.-M. Hu, and Y. Wang, *Phys. Rev. D* **99**, 123002 (2019).
- [64] R. Abbott *et al.* (LIGO Scientific Collaboration and Virgo Collaboration), *Phys. Rev. Lett.* **125**, 101102 (2020).
- [14] L. C. Stein and N. Warburton, *Phys. Rev. D* **101**, 064007 (2020).
- [66] N. I. Shakura and R. A. Sunyaev, *Astron. Astrophys.* **24**, 337 (1973).
- [67] S. A. Teukolsky, *Phys. Rev. Lett.* **29**, 1114 (1972).
- [68] S. A. Teukolsky, *Astrophys. J.* **185**, 635 (1973).
- [69] S. A. Teukolsky and W. H. Press, *Astrophys. J.* **193**, 443 (1974).
- [70] J. B. Hartle and D. C. Wilkins, *Communications in Mathematical Physics* **38**, 47 (1974).
- [71] M. Sasaki and T. Nakamura, *Physics Letters A* **89**, 68 (1982).
- [72] M. Sasaki and T. Nakamura, *Progress of Theoretical Physics* **67**, 1788 (1982).
- [73] S. Chandrasekhar and S. Detweiler, *Proceedings of the Royal Society of London Series A* **344**, 441 (1975).
- [74] E. Poisson, *Phys. Rev. D* **47**, 1497 (1993).
- [75] C. Cutler, L. S. Finn, E. Poisson, and G. J. Sussman, *Phys. Rev. D* **47**, 1511 (1993).
- [76] T. Apostolatos, D. Kennefick, A. Ori, and E. Poisson, *Phys. Rev. D* **47**, 5376 (1993).
- [77] E. Poisson, *Phys. Rev. D* **48**, 1860 (1993).
- [78] E. Poisson and M. Sasaki, *Phys. Rev. D* **51**, 5753 (1995).
- [79] S. Mano, H. Suzuki, and E. Takasugi, *Progress of Theoretical Physics* **95**, 1079 (1996).
- [80] S. Mano and E. Takasugi, *Progress of Theoretical Physics* **97**, 213 (1997).
- [81] M. Campanelli and C. O. Lousto, *Phys. Rev. D* **56**, 6363 (1997).
- [82] S. A. Hughes, *Phys. Rev. D* **62**, 044029 (2000).
- [83] R. K. L. Lo, *Phys. Rev. D* **110**, 124070 (2024).
- [84] E. Newman and R. Penrose, *J. Math. Phys.* **3**, 566 (1962).
- [85] R. P. Geroch, A. Held, and R. Penrose, *J. Math. Phys.* **14**, 874 (1973).
- [86] A. Held, *Communications in Mathematical Physics* **44**, 211 (1975).
- [9] L. Barack and C. Cutler, *Phys. Rev. D* **69**, 082005 (2004).
- [10] S. Babak, H. Fang, J. R. Gair, K. Glampedakis, and S. A. Hughes, *Phys. Rev. D* **75**, 024005 (2007).
- [11] A. J. Chua and J. R. Gair, *Class. Quant. Grav.* **32**, 232002 (2015).
- [12] A. J. K. Chua, C. J. Moore, and J. R. Gair, *Phys. Rev. D* **96**, 044005 (2017).
- [13] A. J. K. Chua, C. R. Galley, and M. Vallisneri, *Phys. Rev. Lett.* **122**, 211101 (2019).
- [15] R. Fujita and M. Shibata, *Phys. Rev. D* **102**, 064005 (2020).
- [16] A. J. K. Chua, M. L. Katz, N. Warburton, and S. A. Hughes, *Phys. Rev. Lett.* **126**, 051102 (2021).
- [17] M. L. Katz, A. J. K. Chua, L. Speri, N. Warburton, and S. A. Hughes, *Phys. Rev. D* **104**, 064047 (2021).
- [19] L. Speri, M. L. Katz, A. J. K. Chua, S. A. Hughes, N. Warburton, J. E. Thompson, C. E. A. Chapman-Bird, and J. R. Gair, *Frontiers in Applied Mathematics and Statistics* **9**, 10.3389/fams.2023.1266739 (2024).
- [6] W. Schmidt, *Classical and Quantum Gravity* **19**, 2743 (2002).
- [7] S. A. Hughes, *Phys. Rev. D* **109**, 064077 (2024).

- [98] B. Carter, *Phys. Rev.* **174**, 1559 (1968).
- [99] J. M. Bardeen, W. H. Press, and S. A. Teukolsky, *Astrophys. J.* **178**, 347 (1972).
- [100] E. E. Flanagan and T. Hinderer, *Phys. Rev. D* **75**, 124007 (2007).
- [101] See Supplemental Material at [URL will be inserted by publisher] for the derivation of the Jacobian.
- [20] E. S. C. Ching, P. T. Leung, W. M. Suen, and K. Young, *Phys. Rev. Lett.* **74**, 2414 (1995).
- [21] W.-B. Han and X. Chen, *Monthly Notices of the Royal Astronomical Society: Letters* **485**, L29 (2019).
- [24] T. Islam, G. Faggioli, G. Khanna, S. E. Field, M. van de Meent, and A. Buonanno, *Phenomenology and origin of late-time tails in eccentric binary black hole mergers* (2024), [arXiv:2407.04682 \[gr-qc\]](#).
- [105] M. Giustini *et al.*, *Astronomy & Astrophysics* **692**, A15 (2024).
- [106] L. S. Finn, *Phys. Rev. D* **46**, 5236 (1992).
- [107] S. Babak *et al.*, *Phys. Rev. D* **95**, 103012 (2017).
- [108] B. J. Owen, *Phys. Rev. D* **53**, 6749 (1996).
- [109] S. D. Mohanty, *Phys. Rev. D* **57**, 630 (1998).
- [110] M. Pürrer and C.-J. Haster, *Phys. Rev. Res.* **2**, 023151 (2020).
- [111] E. Pizzati, S. Sachdev, A. Gupta, and B. S. Sathyaprakash, *Phys. Rev. D* **105**, 104016 (2022).
- [112] C. Cutler and M. Vallisneri, *Phys. Rev. D* **76**, 104018 (2007).
- [113] M. Van De Meent and N. Warburton, *Class. Quant. Grav.* **35**, 144003 (2018).
- [114] P. Lynch, M. van de Meent, and N. Warburton, *Class. Quant. Grav.* **39**, 145004 (2022).
- [115] P. Lynch, M. van de Meent, and N. Warburton, *Phys. Rev. D* **109**, 084072 (2024).
- [116] L. V. Drummond, P. Lynch, A. G. Hanselman, D. R. Becker, and S. A. Hughes, *Phys. Rev. D* **109**, 064030 (2024).
- [117] P. Lynch, V. Witzany, M. van de Meent, and N. Warburton, *Class. Quant. Grav.* **41**, 225002 (2024).
- [118] R. Arcodia *et al.*, *Astronomy & Astrophysics* **690**, A80 (2024).
- [119] S. A. Hughes, *Phys. Rev. D* **100**, 064001 (2019).

**Supplementary Material to Lui, Torres-Orjuela, Chowdhury, & Dai (2025).
Gravitational Wave Signatures of Quasi-Periodic Eruptions:
LISA Detection Prospects for RX J1301.9+2747**

Evolution of Orbital Parameters with Disk Collisions

For a Kerr black hole of mass M and spin $a \leq |M|$, the equations of motion (EOM) in Boyer-Linquist coordinates (t, r, θ, ϕ) are as follows [1–5]

$$\left(\frac{dr}{d\lambda}\right)^2 = [\mathcal{E}(r^2 + a^2) - a\mathcal{L}_z]^2 - \Delta [r^2 + (\mathcal{L}_z - a\mathcal{E})^2 + \mathcal{Q}] \equiv V_r(r), \quad (15)$$

$$\left(\frac{d\theta}{d\lambda}\right)^2 = \mathcal{Q} - \mathcal{L}_z \cot^2 \theta - a^2(1 - \mathcal{E}^2) \cos^2 \theta \equiv V_\theta(\theta), \quad (16)$$

$$\frac{d\phi}{d\lambda} = \mathcal{L}_z \csc^2 \theta - \frac{a}{\Delta} (\mathcal{L}_z - 2Ma\mathcal{E}), \quad (17)$$

$$\frac{dt}{d\lambda} = \mathcal{E} \left[\frac{(r^2 + a^2)}{\Delta} - a^2 \sin^2 \theta \right] - \frac{2Mar\mathcal{L}_z}{\Delta}, \quad (18)$$

where λ is the Mino-Carter time [1] and $(\mathcal{E}, \mathcal{L}_z, \mathcal{Q})$ are the constants of motion. To find the turning points, we need to solve the equation $V_r = 0$, which yields four roots $r_1 > r_2 > r_3 > r_4$ [3, 4, 6]. For stable eccentric orbits, $r_1 = r_a$ and $r_2 = r_p$, which are the apocenter and pericenter radius, respectively, given by [7]

$$r_a = -2\sqrt{\mathcal{Q}} \cos\left(\frac{\theta + 2\pi}{3}\right) - \frac{A_2}{3}, \quad r_p = -2\sqrt{\mathcal{Q}} \cos\left(\frac{\theta - 2\pi}{3}\right) - \frac{A_2}{3}, \quad (19)$$

$$\mathcal{Q} = \frac{1}{9} (A_2^2 - 3A_1), \quad \mathcal{R} = \frac{1}{54} (2A_2^3 - 9A_2A_1 + 27A_0), \quad (20)$$

$$A_0 = \frac{2M(aE - L_z)^2}{E^2 - 1}, \quad A_1 = \frac{a^2(E^2 - 1) - L_z^2}{E^2 - 1}, \quad A_2 = \frac{2M}{E^2 - 1}. \quad (21)$$

Using Eq. (19) and (21), one can define a semi-latus rectum p and an orbital eccentricity e

$$p = \frac{2r_a r_p}{r_a + r_p}, \quad e = \frac{r_a - r_p}{r_a + r_p}. \quad (22)$$

Similarly, to determine the angular turning points, we solve for the polar roots when $V_\theta = 0$. The polar EOMs can be rewritten in terms of the cosine of the inclination angle x_I [7]

$$V_\theta(x_I) = a^2(1 - \mathcal{E}^2)x_I^2 + [\mathcal{Q} + \mathcal{L}_z - a^2(1 - \mathcal{E}^2)]x_I^2 - \mathcal{L}_z^2, \quad (23)$$

and solving for the x_I yields

$$x_I = \sqrt{\frac{\mathcal{Q} + \mathcal{L}_z^2 - a^2(1 - \mathcal{E}^2) \pm \sqrt{(\mathcal{Q} + \mathcal{L}_z^2 - a^2(1 - \mathcal{E}^2))^2 + 4a^2\mathcal{L}_z^2(1 - \mathcal{E}^2)}}{2a^2(1 - \mathcal{E}^2)}}, \quad (24)$$

Hence, one can reparametrize the EOM using the quasi-Keplerian coordinates (p, e, x_I) , and their expression as a function of $(\mathcal{E}, \mathcal{L}_z, \mathcal{Q})$ [3, 6]. This parameterization is used in the **FastEMRIWaveforms** software package when evolving the inspiral due to gravitational radiation.

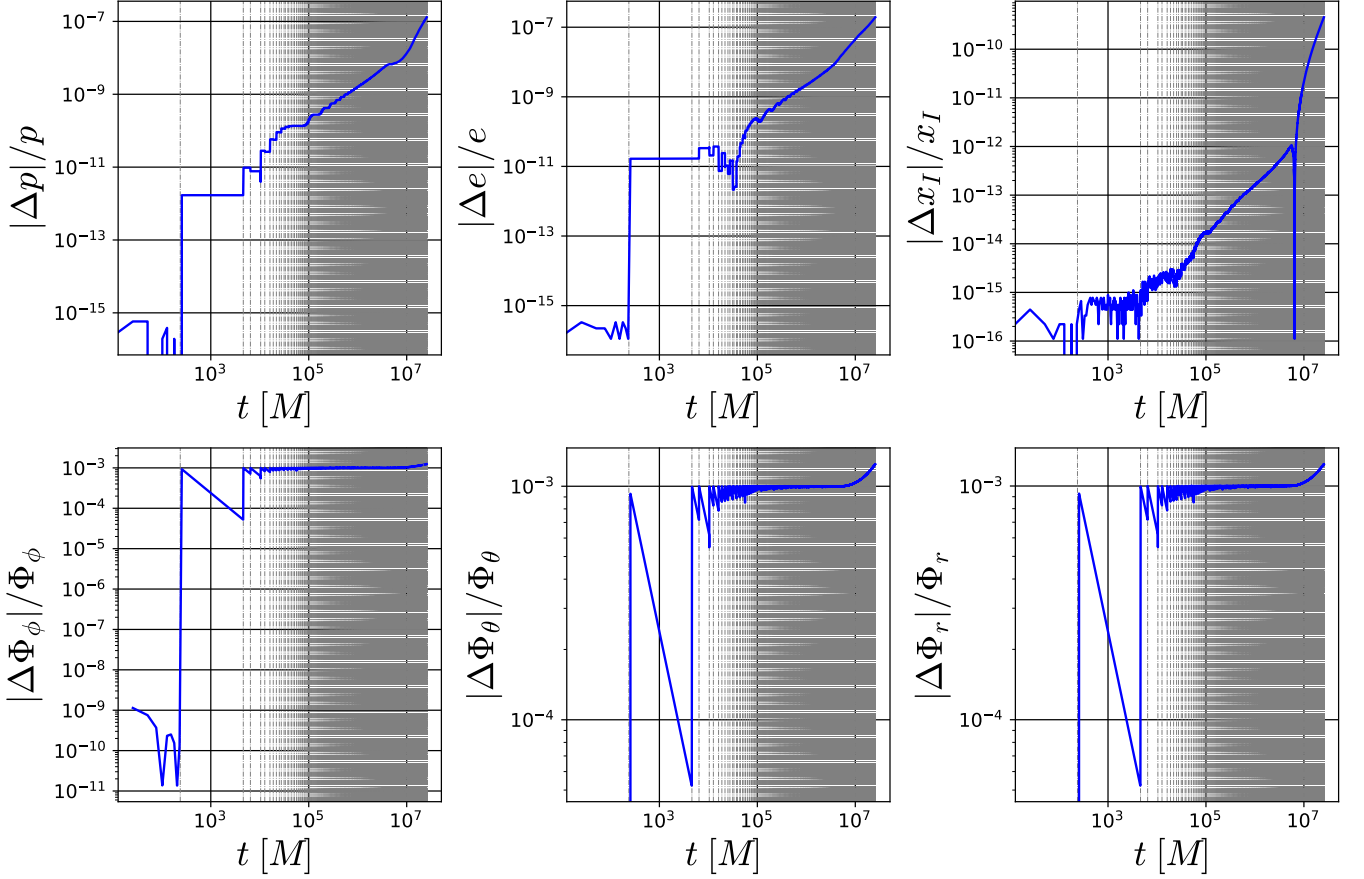


FIG. 5. The relative difference in orbital parameters between a QPE EMRI perturbed by ODIs and a vacuum EMRI ($|\Delta p|/p$, $|\Delta e|/e$, $|\Delta x_I|/x_I$, $|\Delta \Phi_{r,\theta,\phi}|/\Phi_{r,\theta,\phi}$), where $\Delta \mathcal{O} = \mathcal{O}' - \mathcal{O}$ is the difference between the ODI perturbed orbiter parameters \mathcal{O}' and vacuum orbital parameters \mathcal{O} . The initial conditions for the orbit are $p_0 = 73.5M(1 - e_0^2)$, $e_0 = 0.25$, $x_{I0} = 0.5$, $\Phi_{r0} = \Phi_{\theta0} = \Phi_{\phi0} = 0$, and the BH masses and spins are $M = 10^6 M_\odot$, $\mu = 30 M_\odot$, and $a = 0.9$. The gray dash-dotted lines indicate the times when ODIs occur.

To determine the change in quasi-Keplerian coordinates due to orbiter-disk interactions, we define a two vectors $\mathcal{K}_i = (p, e, x_I)$ and $\mathcal{C}_i = (\mathcal{E}, \mathcal{L}_z, \mathcal{Q})$, which are related by $\delta \mathcal{K}_i = \frac{\partial \mathcal{K}_i}{\partial \mathcal{C}_j} \delta \mathcal{C}_j$ and can be written as a Jacobian that forms a system of equations

$$\begin{pmatrix} \delta p \\ \delta e \\ \delta x_I \end{pmatrix} = \begin{pmatrix} \frac{\partial p}{\partial \mathcal{E}} & \frac{\partial p}{\partial \mathcal{L}_z} & \frac{\partial p}{\partial \mathcal{Q}} \\ \frac{\partial e}{\partial \mathcal{E}} & \frac{\partial e}{\partial \mathcal{L}_z} & \frac{\partial e}{\partial \mathcal{Q}} \\ \frac{\partial x_I}{\partial \mathcal{E}} & \frac{\partial x_I}{\partial \mathcal{L}_z} & \frac{\partial x_I}{\partial \mathcal{Q}} \end{pmatrix} \begin{pmatrix} \delta \mathcal{E} \\ \delta \mathcal{L}_z \\ \delta \mathcal{Q} \end{pmatrix}. \quad (25)$$

Note that this equation is underdetermined, and we need to impose two conditions to solve for $\delta \mathcal{K}_i$. The first condition we impose is $\delta r = 0$, as we do not want the stellar-mass orbiter (SMO) to suddenly change radial position after each disk collision. Therefore, $\delta p = p \cdot \delta e \cos \psi / (1 + \cos \psi)$, as $r = p / (1 + e \cos \psi)$. The second condition we impose is $\delta x_I = 0$, because we assume that the collision angle I is constant during the encounter, as the disk is thin and will only damp the SMO's velocity without changing its direction. This approximation is valid in the supersonic regime, where the SMO's velocity is much greater than the velocity of the gas in the disk [8].

In the main paper, we compare the orbital evolution of an extreme mass-ratio inspiral (EMRI) driven purely by gravitational wave (GW) emission with an EMRI additionally influenced by orbital disk interactions (ODIs). ODIs are modeled as impulsive energy dissipation from dynamical friction shocks, governed by Eq. (1) and (2) of the main paper. In FIG. 5, we compare the orbital evolution of a QPE EMRI perturbed by ODIs with a vacuum EMRI by plotting the difference in orbital parameters over time. Observe that the deviation between the orbital evolution of an ODI perturbed EMRI from the vacuum EMRI increases with the number of disk collisions. From the top panel of FIG. 5, we see the relative differences $|\Delta p|/p$ and $|\Delta e|/e$ are of similar order of magnitude ($\sim 10^{-7}$) whereas the

$|\Delta x_I|/x_I$ is much smaller ($\sim 10^{-10}$). This is consistent with the way we update the orbital parameters, as updating p and e whilst keeping x_I after each ODI would not change x_I significantly. However, this would change the way x_I evolves due to GW radiation between QPE bursts, as each ODI induces a change in the constants of motion ($\mathcal{E}, \mathcal{L}_z, \mathcal{Q}$). The cumulative effects of ODIs cause the orbit to inspiral and circularize more rapidly than vacuum EMRIs due to reduced energy and angular momentum. This is further supported by the accelerated orbital phase in the bottom panel of FIG. 5, as the relative difference of the GW phase $|\Delta\Phi_{r,\theta,\phi}|/\Phi_{r,\theta,\phi}$ also increases with the number of ODIs. The reason for this is an accelerated decrease in p and e causing an increase in the GW fundamental frequencies $\Omega_{r,\theta,\phi}$, where $\Phi_{r,\theta,\phi}(t) = \int_0^t \Omega_{r,\theta,\phi}(p, e, x_I) dt'$. This process is explained in greater detail in the main paper.

Non-Discrete Modes and High-Frequency Tails

To model the gravitational waveform from an EMRI with ODIs, we consider a time-domain signal $h(t)$ experiencing impulsive changes in amplitude and frequency at collision times t_c

$$h(t) = \frac{\mu}{d_L} S(\theta, \phi) \begin{cases} \mathcal{A} e^{-i\Phi_{\text{pre}}(t)}, & t < t_c, \\ (\mathcal{A} + \delta\mathcal{A}) e^{-i\Phi_{\text{post}}(t)}, & t \geq t_c, \end{cases} \quad (26)$$

where $\Phi_{\text{pre/post}}(t)$ are the orbital phases before and after the ODI, and $\omega(t) = \dot{\Phi}(t)$ undergoes a discontinuity $\delta\omega$ at t_c . The Fourier transform $\tilde{h}(f)$ is given by

$$\tilde{h}(f) = \int_{-\infty}^{\infty} h(t) e^{-i2\pi f t} dt = \frac{\mu}{d_L} S(\theta, \phi) [\mathcal{I}_{\text{pre}} + \mathcal{I}_{\text{post}} + \mathcal{I}_{\text{jump}}]. \quad (27)$$

For the smooth portions of the waveform ($t \neq t_c$), we evaluate \mathcal{I}_{pre} and $\mathcal{I}_{\text{post}}$ using the stationary phase approximation (SPA). This method applies when the phase is rapidly varying, with dominant contributions at times where the derivative of the total phase vanishes

$$\frac{d}{dt} [\Phi_{\text{pre/post}}(t) + 2\pi f t] = \omega_{\text{pre/post}}(t) - 2\pi f = 0. \quad (28)$$

The SPA yields quasi-monochromatic peaks $G_{\text{pre}}(f)$ and $G_{\text{post}}(f)$ centered at the orbital frequencies before and after the sudden frequency shift caused by the ODI.

The abrupt frequency change at t_c creates a discontinuity in the waveform's derivative. To derive the high-frequency asymptotic behavior, we analyze the phase perturbation using the Sokhotski-Plemelj theorem. Consider the phase difference induced by the ODI

$$\Psi(t) = e^{-i[\Phi(t) - \Phi_0(t)]} = e^{-i\Delta\omega \cdot (t - t_c) H(t - t_c)}, \quad (29)$$

where $\Phi_0(t)$ is the unperturbed phase and $H(t - t_c)$ is the Heaviside function. The Fourier transform of $\Psi(t)$ is

$$\tilde{\Psi}(f) = \int_{-\infty}^{\infty} e^{-i\Delta\omega(t - t_c) H(t - t_c)} e^{-i2\pi f t} dt = \int_{-\infty}^{t_c} e^{-i2\pi f t} dt + \int_{t_c}^{\infty} e^{-i[\Delta\omega(t - t_c) + 2\pi f t]} dt. \quad (30)$$

The post-ODI integral contains the essential discontinuity and can be rewritten by substituting $\tau = t - t_c$. Applying the Sokhotski-Plemelj theorem to evaluate this distributional integral gives

$$\mathcal{I}_{\text{post}} = e^{-i2\pi f t_c} \int_0^{\infty} e^{-i(\Delta\omega + 2\pi f)\tau} d\tau = \lim_{\epsilon \rightarrow 0^+} \int_0^{\infty} e^{-i(\alpha + i\epsilon)\tau} d\tau = -\mathcal{P}\left(\frac{1}{\alpha}\right) + i\pi\delta(\alpha), \quad \alpha \equiv \Delta\omega + 2\pi f. \quad (31)$$

For the high-frequency tail, when $|f|$ is much larger than $|\Delta\omega|/2\pi$, the principal value term dominates

$$\mathcal{I}_{\text{post}} \approx -e^{-i2\pi f t_c} \mathcal{P}\left(\frac{1}{2\pi f}\right) \sim -\frac{e^{-i2\pi f t_c}}{2\pi f}. \quad (32)$$

Thus, the full discontinuity contribution asymptotically behaves as $\tilde{\Psi}(f) \sim -e^{-i2\pi f t_c}/(2\pi f)$ as $f \rightarrow \infty$. The $1/f$ decay is characteristic of waveform discontinuities. For amplitude jumps, an identical analysis yields

$$\mathcal{I}_{\text{jump}} = \frac{\delta\mathcal{A}}{i2\pi f} e^{-i[\Phi(t_c) + 2\pi f t_c]}. \quad (33)$$

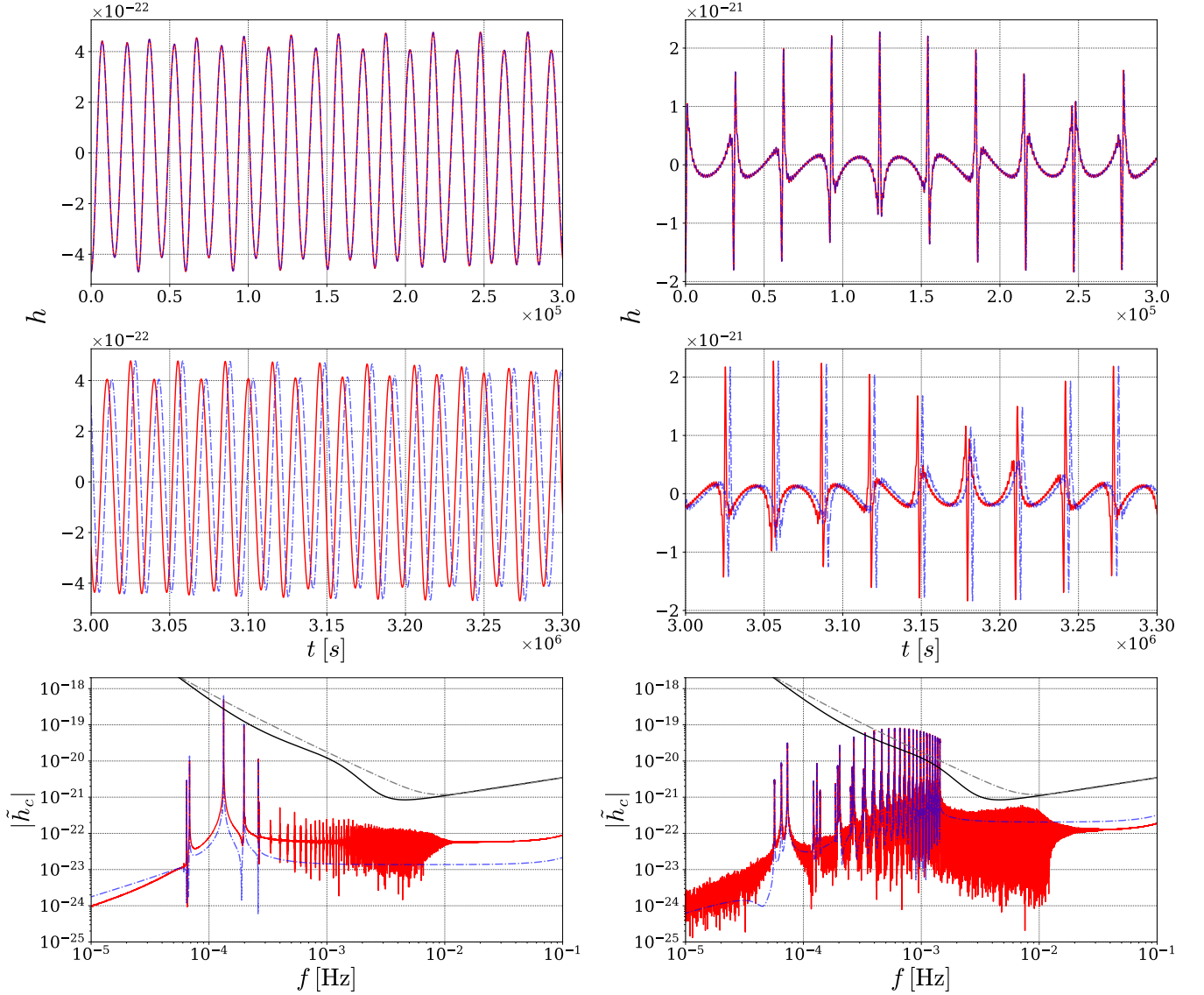


FIG. 6. Strain (top 2 panels) and characteristic strain (bottom panel) of a vacuum EMRI (dashed blue line) versus an EMRI with ODIs (solid red line) for eccentricities of $e_0 = 0.05$ (left plots) and $e_0 = 0.75$ (right plots). The dashed green lines indicate the occurrence of an ODI. The full TD waveform is not shown to avoid clutter and is truncated to show the waveform at early and late times. The initial parameters are $M = 10^6 M_\odot$, $\mu = 30 M_\odot$, $a = 0.9$, $p_0 = 15M(1 - e_0^2)$, $x_{I0} = 0.5$, $\Phi_\phi = \Phi_\theta = \Phi_r = 0$, $q_K = \phi_K = q_S = \phi_S = 0.01$, and $d_L = 0.1$ Mpc

Frequency jumps, $\delta\omega$, produce discontinuities in $\dot{h}(t)$, generating a $1/f^2$ term through the relation $\mathcal{F}[\dot{h}(t)] = i2\pi f \tilde{h}(f)$. Combining all components, the asymptotic spectrum is

$$\tilde{h}(f) = \frac{\mu}{d_L} S(\theta, \phi) \left[\underbrace{\mathcal{A}G_{\text{pre}}(f) + (\mathcal{A} + \delta\mathcal{A})G_{\text{post}}(f)}_{\text{SPA quasi-monochromatic peaks}} + \underbrace{\frac{\delta\mathcal{A}}{2\pi i f} e^{-i[\Phi(t_c) + 2\pi f t_c]}}_{\sim 1/f} - \underbrace{\frac{i\mathcal{A}\delta\omega}{(2\pi f)^2} e^{-i[\Phi(t_c) + 2\pi f t_c]}}_{\sim 1/f^2} \right], \quad (34)$$

where the quasi-monochromatic peaks from SPA are captured by $G_{\text{pre}}(f)$ and $G_{\text{post}}(f)$, while the amplitude and frequency jumps produce the high-frequency tails proportional to $1/f$ and $1/f^2$, respectively. These tails enhance detectability by increasing the power spectrum in the sensitivity band of space-based GW detectors such as LISA.

In FIG. 6, we compute the GW strain and frequency spectra (characteristic strain) for EMRIs with ODIs using the **FastEMRIWaveforms** software package [9–19], and compare the waveform with EMRIs in vacuum for different eccentricities. The top panel shows the two signals initially in phase with little amplitude deviation. However, the

middle panel reveals a gradual drift in phase and divergence in amplitude due to accumulated energy and angular momentum reductions from ODIs. The bottom panels show the characteristic strain $|h_c(f)| = 2f|\tilde{h}(f)|$. In the frequency domain, the impulsive reductions produce a high-frequency tail and excite non-discrete GW modes. EMRIs with ODIs generate broadband spectral content between the harmonic peaks characteristic of vacuum EMRIs, corresponding to transient GW emission during ODIs. This fills frequency bands that traditionally remain quiet in vacuum EMRIs. Most significantly, the $1/f$ and $1/f^2$ asymptotic tails increases $|h_c|$. This high-frequency tail arises from constructive interference of discontinuity contributions across multiple collision times t_c . The combined effect of non-discrete mode excitation and high-frequency tails substantially enhances detectability prospects by increasing the characteristic strain in the band of LISA, TianQin, and Taiji [20–24].

-
- [1] Y. Mino, Perturbative approach to an orbital evolution around a supermassive black hole, *Phys. Rev. D* **67**, 084027 (2003).
 - [2] S. Drasco and S. A. Hughes, Rotating black hole orbit functionals in the frequency domain, *Phys. Rev. D* **69**, 044015 (2004).
 - [3] R. Fujita and W. Hikida, Analytical solutions of bound timelike geodesic orbits in kerr spacetime, *Classical and Quantum Gravity* **26**, 135002 (2009).
 - [4] M. van de Meent, Analytic solutions for parallel transport along generic bound geodesics in kerr spacetime, *Classical and Quantum Gravity* **37**, 145007 (2020).
 - [5] C. Dyson and M. van de Meent, Kerr-fully diving into the abyss: analytic solutions to plunging geodesics in kerr, *Classical and Quantum Gravity* **40**, 195026 (2023).
 - [6] W. Schmidt, Celestial mechanics in kerr spacetime, *Classical and Quantum Gravity* **19**, 2743 (2002).
 - [7] S. A. Hughes, Parameterizing black hole orbits for adiabatic inspiral, *Phys. Rev. D* **109**, 064077 (2024).
 - [8] F. Duque, S. Kejriwal, L. Sberna, L. Speri, and J. Gair, Constraining accretion physics with gravitational waves from eccentric extreme-mass-ratio inspirals, *Phys. Rev. D* **111**, 084006 (2025).
 - [9] L. Barack and C. Cutler, LISA capture sources: Approximate waveforms, signal-to-noise ratios, and parameter estimation accuracy, *Phys. Rev. D* **69**, 082005 (2004).
 - [10] S. Babak, H. Fang, J. R. Gair, K. Glampedakis, and S. A. Hughes, “Kludge” gravitational waveforms for a test-body orbiting a Kerr black hole, *Phys. Rev. D* **75**, 024005 (2007).
 - [11] A. J. Chua and J. R. Gair, Improved analytic extreme-mass-ratio inspiral model for scoping out eLISA data analysis, *Class. Quant. Grav.* **32**, 232002 (2015).
 - [12] A. J. K. Chua, C. J. Moore, and J. R. Gair, Augmented kludge waveforms for detecting extreme-mass-ratio inspirals, *Phys. Rev. D* **96**, 044005 (2017).
 - [13] A. J. K. Chua, C. R. Galley, and M. Vallisneri, Reduced-Order Modeling with Artificial Neurons for Gravitational-Wave Inference, *Phys. Rev. Lett.* **122**, 211101 (2019).
 - [14] L. C. Stein and N. Warburton, Location of the last stable orbit in Kerr spacetime, *Phys. Rev. D* **101**, 064007 (2020).
 - [15] R. Fujita and M. Shibata, Extreme mass ratio inspirals on the equatorial plane in the adiabatic order, *Phys. Rev. D* **102**, 064005 (2020).
 - [16] A. J. K. Chua, M. L. Katz, N. Warburton, and S. A. Hughes, Rapid Generation of Fully Relativistic Extreme-Mass-Ratio-Inspiral Waveform Templates for LISA Data Analysis, *Phys. Rev. Lett.* **126**, 051102 (2021).
 - [17] M. L. Katz, A. J. K. Chua, L. Speri, N. Warburton, and S. A. Hughes, Fast extreme-mass-ratio-inspiral waveforms: New tools for millihertz gravitational-wave data analysis, *Phys. Rev. D* **104**, 064047 (2021).
 - [18] M. L. Katz, L. Speri, A. J. K. Chua, C. E. A. Chapman-Bird, N. Warburton, and S. A. Hughes, *BlackHolePerturbationToolkit/FastEMRIWaveforms: Frequency Domain Waveform Added!* (2023).
 - [19] L. Speri, M. L. Katz, A. J. K. Chua, S. A. Hughes, N. Warburton, J. E. Thompson, C. E. A. Chapman-Bird, and J. R. Gair, Fast and Fourier: extreme mass ratio inspiral waveforms in the frequency domain, *Frontiers in Applied Mathematics and Statistics* **9**, 10.3389/fams.2023.1266739 (2024).
 - [20] E. S. C. Ching, P. T. Leung, W. M. Suen, and K. Young, Late-time tail of wave propagation on curved spacetime, *Phys. Rev. Lett.* **74**, 2414 (1995).
 - [21] W.-B. Han and X. Chen, Testing general relativity using binary extreme-mass-ratio inspirals, *Monthly Notices of the Royal Astronomical Society: Letters* **485**, L29 (2019).
 - [22] K. Destounis, A. G. Suvorov, and K. D. Kokkotas, Gravitational wave glitches in chaotic extreme-mass-ratio inspirals, *Phys. Rev. Lett.* **126**, 141102 (2021).
 - [23] M. De Amicis, S. Albanesi, and G. Carullo, Inspiral-inherited ringdown tails, *Phys. Rev. D* **110**, 104005 (2024).
 - [24] T. Islam, G. Faggioli, G. Khanna, S. E. Field, M. van de Meent, and A. Buonanno, *Phenomenology and origin of late-time tails in eccentric binary black hole mergers* (2024), [arXiv:2407.04682 \[gr-qc\]](https://arxiv.org/abs/2407.04682).